FERMILAB-PUB-12-908-APC
ACCEPTED

Superimposed coherent THz wave radiation from mono-energetically bunched multi-beam

Young-Min Shin*

Department of Physics, Northern Illinois University, Dekalb, IL, 60115, USA

Accelerator Physics Center (APC), Fermi National Accelerator Laboratory (FNAL), Batavia, IL, 60510, USA

Abstract

Intense coherent radiation is obtained from multiple electron beams monochromatically bunched over the wide higher-order-mode (HOM) spectral band in the THz regime. The overmoded waveguide corrugated by dielectric-implanted staggered gratings superimposes evanescent waves emitted from the low energy electron beams. The dispersion and transmission simulations of the three-beam slow wave structure show that the first two fundamental modes (TE_{10} and TE_{20}) are considerably suppressed (~ − 50 dB) below the multi-beam resonating mode (TE_{30}) at the THz regime (0.8 − 1.24 THz). The theoretical calculations and particle-in-cell simulations show that with significantly higher interaction impedance and power growth rate radiation of the TE_{30} mode is ~ 23 dBm and ~ 50 dBm stronger than the TE_{10} and TE_{20} modes around 1 THz, respectively. This highly selective HOM multi-beam interaction has potential applications for power THz sources and high intensity accelerators.

Key word: higher-order-mode, overmode, THz, multi-beam, source, accelerator

* yshin@niu.edu

Operated by Fermi Research Alliance, LLC under Contract No. De-AC02-07CH11359 with the United States Department of Energy

For many decades, radiation kinematics of charged particles has been intriguing subject so as to be widely studied in the fields of particle accelerators and light sources. An often raised underlying question has been how to increase the quantum efficiency of electron-photon conversion in a feasible manner over the broad energy spectrum. In general, rotational and vibrational motions of accelerating charges produce high energy synchrotron and braking radiations[1 – 3] whereas generally the two-dimensional particle motions need large physical volume to induce photon emissions. On the other hand, a linearly co-propagating charge-wave interaction[4 – 6] fits in a small scale with high energy conversion efficiency; it has long been used for microwave generation, although low energy electrons normally produce lower energy photons. Owing to efficient energy conversion and robust thermal capacity, the one-dimensionally polarized electron beam has been recently considered for THz wave source applications[7, 8]. Apparently, the radiation from the linear beam is appreciably more powerful when it is coherent. This, however, requires very high current density ($\propto \lambda^{-2}$) for the beam modulation in the THz regime[9]. The high density of the charge bunches leads to growth of the beam emittance due to increasing space charge force, which can then cause abnormal beam-wave interaction[10, 11]. The beam would thus need to be immersed in a high magnetic field flux to compensate for the divergent defocusing force, thereby rendering the system bulky. Seeding a driving signal for the stimulated emission can significantly lower the current density threshold; THz band, however, lacks an available input driving source. Relevant to the issue, the multi-beam interaction concept has been considered to be a substantial solution to reducing charge density as well as to increasing radiation intensity[12 – 15]. It may nevertheless excite multiple modes, which could cause unstable overmoding problems such as mode-competition/conversion and parasite oscillation. Among several HOM filtering schemes[16 – 18] dielectric implantation[19] is distinctly advantageous for selecting a multi-beam interactive HOM. Embedding equally spaced lossy defects efficiently suppresses all other non-resonating modes, including trapped wakefields. Although this approach

is feasible for achieving high power radiation by increasing the number of beams, its practical THz application is still challenging for related technical and physical issues.

This paper presents broadband coherent radiation from multi-beams HOM interaction, inducing power multiplication at the THz range. The quasi-optically filtered HOM slow wave structure (SWS), consisting of the staggered double grating array (SDGA)[20] with the dielectric-lattices, is proposed to multiply radiation intensity by HOM-superposition of guided radiations from individual beams (See Fig. 1(a)). The SDGAed waveguide has been most intensively studied for G-band (0.2 ~ 0.3 THz) source development due to its large intrinsic bandwidth of high energy efficiency[21]. This paper will present theoretical analysis and particle-in-cell (PIC) simulation results demonstrating a Watt level THz radiation from mono-energetically modulated multi-beam with 20 ~ 30 % spectral bandwidth.

For simple proof of concept, the analytic model is designed only with three identical beams. The designed three-beam simulation model has two equi-spaced dielectric plates of Aluminum Nitride with $\varepsilon_r = 20$ and $\tan\delta = 0.25$. The electrical conductivity of the waveguide is $\sigma = 5.8\times10^7$ [$\Omega^{-1}m^{-1}$], corresponding to that of OFHC copper. For a mid-band frequency (f_{TE30} ~ 1 THz), normalized dimensions of the designed structure are $L = 0.6d$, $a = 0.345d$, $b = 0.33d$, and $h = 1.7d$. It is thus anticipated that the beams will most dominantly interact with the 3rd harmonic mode (TE_{30}). The main role of the lossy defects is to maximize attenuation of the lower order modes (LOMs: TE_{10} and TE_{20}). The beam energy can be intensively concentrated on the TE_{30} mode and not dispersed over the LOMs. The base circuit structure is a staggered double grating arrayed waveguide, as shown in Figure 1(b). While allowing an operating HOM to travel through the circuit with minimal loss, the lossy dielectric rods strongly attenuate all other non-resonant fields, including white background noises. The half-period staggering of a pair of 1-D vane

arrays accommodates a strong constructive longitudinal electric field distribution of the HOM along the direction of the electron beam propagation. This mode of the staggered vane structure has a symmetric field distribution with has a sinusoidal phase variation along the axial direction.

In Fig. 2(a), the beam line intersects the 1st spatial harmonic dispersion curves (m = 1) of the three fundamental modes in two or three points according to beam energies, calculated using finite-integral-technique (FIT) eigenmode solver[22]. The structural dimensions are designed to provide a broad bandwidth and large transverse dimensions to allow high power operation. The dimensional parameters have been optimized to achieve a wide instantaneous bandwidth of ~ 0.2 THz (~28%). For the sake of clarification, φ (normalized phase change = kd) = 1 ~ 2π and 2 ~ 3π is denoted to be the backward and forward wave regimes, respectively. Figure 2(b) shows the phase velocity (υ_p (ω) = $\omega d/\varphi$: bottom) and corresponding synchronized beam voltage ($V_e(\omega)$: top) versus frequency graphs of the backward (LHS: φ = 1 ~ 2π) and forward (RHS: φ = 2 ~ 3π) wave bands, computed from $V_e(\omega) = \frac{\upsilon_p}{\sqrt{1-\upsilon_p^2}} V_n$, where $V_n = m_e c^2/e = 5.11 \times 10^5$ [V] and d is the grating period. Note that matching phase velocities for the beam-wave synchronization increase rapidly up to φ = π (coalesced mode) along the fundamental passbands (solid lines), but they drop along the 2nd order passbands (dotted lines) at φ = 1 ~ 2π (LHS). On the other hand, the velocities (and beam voltage) continue to rise from the fundamental to 2nd band at φ = 2 ~ 3π (RHS). One can see that with the fundamental passbands, forward wave amplification requires much lower beam power than backward wave oscillation for coherent radiation. Notwithstanding, the amplification needs an input driving source that seldom, if ever,

exists in the THz range, whereas the former have broader spectral matching with a beam than the latter. In Fig. 2(b), since the beam crossing over all three passbands could concurrently excite all three waveguide modes, the TE_{10} and TE_{20} modes would dominantly oscillate. The electron energies could thus disperse over the LOMs, which could cause poor energy conversion in the TE_{30} mode operation with three beams. Inserting the two equi-spaced dielectric rods impose huge energy absorption on the two non-resonating modes to prevent the LOM oscillation.

Figure 3 shows transmission characteristics (S_{21}) and EM power distribution (poynting vector) plots of 1.8 mm long waveguide (30 cells) with and without dielectric loading. In the absence of dielectric loading the three modes have nearly the same amount of insertion losses, ~ - 0.4 dB (= ~ 0.22 dB/mm, TE_{10}), ~ - 1 dB (= ~ 0.55 dB/mm, TE_{20}), and ~ -1.4 dB (= ~ 0.78 dB/mm). Over the frequency range (~ 1 THz) where these three passbands heavily overlap, the three slow wave modes are thus strongly competing. However, the transmission graph of the dielectric-loaded waveguide in Fig. 3(a) clearly shows that with the inclusion of dielectric loading the two lower modes are suppressed down to ~- 63 dB (~35 dB/mm, TE_{10}) and ~ -80 dB (~ 44.4 dB/mm, TE_{20}). On the contrary, the TE_{30} mode appears to have no reduction of signal transmission even with these dielectrics (~ - 4 dB: ~ 2.2 dB/mm). The rods intensively distort the field distributions of the two lower modes (TE_{10} and TE_{20}), while the TE_{30} mode (designed operating mode) has no change with the lossy dielectrics. It should be noted that the positions of the dielectric plates are exactly matched with the nodes of the TE_{30} mode, so that the field distribution is not disturbed by insertion of the defects. This overwhelming mode suppression is also reflected in the cavity parameters. In Fig. 4, the cavity

impedance (R/Q) and quality factor (Q_0) versus frequency graphs obtained from eigenmode simulations. In the simulation, R/Qs were calculated at the transverse position of the maximum electric fields. In Fig. 4(a), R/Qs of the TE_{30} mode and other two LOMs are quite comparable; TE_{10} = 6 – 14 Ω (0.26 ~ 0.91 THz), TE_{20} = 5.5 – 7 Ω (0.5 ~ 1 THz), and TE_{30} = 4.6 – 8.5 Ω (0.8 ~ 1.24 THz). However, at 0.8 ~ 1.24 THz TE_{30} mode has about 5 ~ 25 times higher Q (Q_0 ~ 100 – 250) than LOMs (TE_{10} = 10 – 23, and TE_{20} = 10 – 40). The large amount of EM energy is stored in the space between the loads, which ensure stable single mode operation in the HOM.

Figure 5(a) shows the theoretically estimated Pierce interaction impedance using small signal analysis[23]. This computational approach provides confirmation of the PIC simulation results as well as rapid parameter scans. For the numerical computation, in the simulation code interaction impedance is defined as

$$K_m = \frac{|E_m|^2}{2k_m^2 P} \tag{1}$$

where

$$E_m = \frac{1}{d}\int_0^d E_z(z) e^{ik_m z} dz \tag{2}$$

and P (= $\omega W_E/Q_0$) is the power flow (W_E = 1 Joule: default input energy defined for the eigenmode simulation) and k_m (= $k_0 + 2m\pi/d$) is the propagation constant of the mth space harmonic. As there is no analytic electric field (E_z) model for the multi-beam structure, the field data for the impedance calculation are directly obtained from 3D-EM simulation. Numerical EM simulators use periodic (Master/Slave) boundary conditions for eigenmode solvers. Eigenmodes are thus defined as traveling wave solutions by specifying the phase advance of the periodic boundaries. The solution domain is a single

translational period (d), but the impedances are calculated from the half-period integral as the longitudinal field orientation has 180-degree phase-change at the middle of the defined period. Since the traveling-wave supported by the SDGA structure is represented as a frequency-domain solution in the simulations, the field solution is provided as a full complex-vector field, which directly supports multiplication with the complex exponential in the impedance integral. In order to compare TE_{10}, TE_{20}, and TE_{30} under the same condition, the transverse positions where the electric fields of the modes are maxima are selected for the line-integral in equation (2). Figure 5(a) displays interaction impedance (K_m) versus frequency graph of the backward (top: $\varphi = 1 \sim 2\pi$) and forward (bottom: $\varphi = 2 \sim 3\pi$) wave regimes. At the low energy regime near their lower cutoffs, the dominant TE_{10} and TE_{20} modes have relatively large impedance (0.1 ~ 10 Ω), which therefore compete strongly. However, the impedances fall off steeply with the increase of frequency since energy dissipation due to off-resonance of the LOMs becomes overwhelming. In Fig. 5, although the lower (solid) and upper (dotted) passbands of the two LOMs extend above 1 THz range, their impedances are a few orders of magnitude smaller than that of TE_{30} mode over 0.8 ~ 1.24 THz. The impedances of TE_{10} and TE_{20} modes decrease rapidly with the increase of frequency and become negligibly small in the operating band. On the other hand, the impedance of TE_{30} operating mode continuously increases up to 13 Ω until 1.24 THz. Note that the impedances of TE_{10} and TE_{20} modes fall even more steeply at the forward wave regime ($\varphi = 2 \sim 3\pi$) which has larger wave numbers of lower energy distribution.

The power-flow in the structure is calculated directly from the surface integral of the Poynting vectors in the field solution. The field normalizations are accomplished with an

appropriate power flow or energy calculated from the simulation. The calculated dispersion and impedance values for the fundamental modes are imported into the power growth rate, $\eta = 47.3\left(\frac{\beta_m}{2\pi}\right)C_0$, where $C_0 = \left(\frac{K_m I_0}{4V_0}\right)^{\frac{1}{3}}$ is the Pierce gain parameter. In Fig. 5(b)**,** gain growths are calculated with respect to the frequencies by sweeping the beam voltages, as graphed in Fig. 2(b), with the fixed beam current (I_b = 30 mA). This small signal analysis predicts that the TE_{30} mode achieves gain growths of 8.76 dB/mm and 4.23 dB/mm for the backward (top: $\varphi = 1 \sim 2\ \pi$) and forward wave (bottom: $\varphi = 2 \sim 3\ \pi$) modes at 1 THz, respectively. This gain analysis implies that ideally a 1 cm long circuit can produce 10 W (~ 3.3 W/beam) from 50 nW (backward) and 1.75 mW (forward) driving signals, respectively, with considering the launching loss (= - 9.54 dB). Although the forward wave interaction still appears to require a driving signal of mW-level, gain of the backward wave modes is high so as to strongly bunch the beams exciting coherent radiation from ambient noise seeds. At the lower frequency regime is below the cutoff of TE_{30} band, gain growth rates (η), of the LOMs rise rapidly with decrease of the frequency since a slow beam preserves larger transit time of electron-photon energy transfer, as depicted in the gain parameter, C_0. However, LOM gains noticeably diminish above the TE_{30} cutoff (~ 0.75 THz), while the TE_{30} mode strongly holds 3.5 ~ 4 times higher gain growth rate than LOMs due to relatively lower energy absorption. At 1 THz, a 6 mm long circuit (= 100 periods) is supposed to accommodate 21 ~ 24 times higher power gain to TE_{30} mode over LOMs.

Eventually, THz power multiplication is numerically analyzed by full 3D particle-in-cell (PIC) simulation modeling[24]. Figure 6 shows simulation results from the model with

three identically energized beams that have ~ 67% tunnel-filing ratio. The beam parameters are set to 10 kV, 30 mA with a solenoid focusing field. The simulation demonstrated that the designed circuit produces ~ 2 W (~ 33 dBm, f = 1 THz) of the TE_{30} mode. That is ~ 23 and ~ 50 dBm higher than the TE_{10} and TE_{20} modes, respectively. Also, the low noise spectrum of the TE_{30} mode radiation measured at the output port dominates (+11.4 dB and +26 dB) the output of the TE_{10} and TE_{20} modes. In Fig. 6(c), sidebands of the TE_{30} mode nearly disappear, whereas they distinctly appear at the LOM bands. Each of the fully bunched beams has a 180-degree phase difference with the others as is necessary to interact with the three maxima of the TE_{30} mode. The PIC simulation results also lend credence to the hypothesis that the proposed dielectric loading strongly attenuates the parasitic modes which leads to a clean evolution of the beam under the influence of the input drive signal in the operating LOM. This parasitic mode suppression scheme is simple and suitable for deployment in multiple-beam devices.

In summary, implanting dielectric defects efficiently filter a HOM to synchronize with a multi-beam in the THz regime, which leads to high gain power multiplication. The broadband slow wave structure consisting of the SDGA monochromatically superposes HOM backward waves over the 25% dynamic bandwidth. Theoretical and numerical results corroborate that THz radiation intensity could be further raised with a larger number of beams, indeed lowering the current density threshold for beam modulation. PIC simulation results support the concept that implanting lossy dielectric loads absorbs non-resonating fields so strongly that they have almost no interaction with the electron beams. The coherent HOM multi-beam modulation could be advantageously applicable to coherent radiation sources and high intensity beam accelerators.

References

[1] F. R. Elder, A. M. Gurewitsch, R. V. Langmuir, H. C. Pollock, "Radiation from Electrons in a Synchrotron" Phys. Rev. 71 (11), 829 (1947)

[2] D. J. Griffiths, *Introduction to Electrodynamics*, pp. 463–465

[3] J. K. Knipp, G.E. Uhlenbeck, "Emission of gamma radiation during the beta decay of nuclei". Physica **3** (6): 425 (1936)

[4] G. S. Nusinovich, S. J. Cooke, M. Botton, and B. Levush, Phys. Plasmas **16**, 063102 (2009).

[5] Jin-Kyu So, Jong-Hyo Won, M. A. Sattorov, Seung-Ho Bak, Kyu-Ha Jang, Gun-Sik Park, D. S. Kim, and F. J. Garcia-Vidal, "Cerenkov radiation in metallic metamaterials", Appl. Phys. Lett. **97**, 151107 (2010)

[6] Nusinovich, G.S.; Bliokh, Yu.P.; Abu-Elfadl, T.M., "Cherenkov radiation in vacuum and plasma-filled microwave sources in the absence of guiding magnetic fields", Infrared and Millimeter Waves, 2000. Conference Digest. 25th International conference on, pp. 125 – 126 (2000)

[7] R. L. Ives, IEEE Trans. Plasma Sci. **32**, 1277 (2004)

[8] H. Zhang, J. Wang, C. Tong, X. Li, and G. Wang, Phys. Plasmas **16**, 123104 (2009).

[9] K. Mizuno and S. Ono, J. Appl. Phys. **46**, (1975).

[10] R. B. Miller, J. W. Poukey, B. G. Epstein, S. L. Shope, T. C. Genoni, M. Franz, B. B. Godfrey, R. J. Adler, A. Mondelli, "Beam Transport Issues in High Current Linear Accelerators", IEEE Trans. Nucl. Sci. 28 (3), 3343 (1981)

[11] I. S. Roth, J. D. Ivers, and J. A. Nation, "High Current Ion Beam Generation and Transport System", Appl. Phys. Lett. 46, 251 (1985)

[12] Takuya Ishibashi, Noriyosu Hayashizaki, Toshiyuki Hattori, Taku Ito, Liang Lu, Jun Tamura, "Multibeam cavity for low energy beam acceleration", Nuclear Instruments and Methods in Physics Research B 261 13–16 (2007)

[13] J. H. Booske, R. J. Dobbs, C. D. Joye, C. L. Kory, G. R. Neil, G. S. Park, J. H. Park, and R. J. Temkin, "Vacuum Electronic High Power Terahertz Sources", IEEE Trans. Terahertz Sci. and Tech. 1 (1), 54 (2011)

[14] Gregory S. Nusinovich, Simon J. Cooke, Moti Botton, and Baruch Levush, "Wave coupling in sheet- and multiple-beam traveling-wave tubes", Phys. Plasmas 16 (6), 063102 (2009)

[15] H.P. Freunda,*, D. Douglasb, P.G. O'Sheac, "Multiple-beam free-electron lasers", Nuclear Instruments and Methods in Physics Research A 507 (2003) 373–377

[16] V. Volkov, J. Knobloch and A. Matveenko, "Beam breakup instability suppression in multicell superconducting rf guns", Phys. Rev. ST Accel. Beams 14, 054202 (2011)

[17] E. I. Smirnova, C. Chen, M. A. Shapiro, J. R. Sirigiri, and R. J. Temkin, "Simulation of photonic band gaps in metal rod lattices for microwave applications", J. App. Phys. **91**, 960 (2002)

[18] Evgenya I. Smirnova*, Amit S. Kesar, Ivan Mastovsky, Michael A. Shapiro, and Richard J. Temkin, "Demonstration of a 17-GHz, High-Gradient Accelerator with a Photonic-Band-Gap Structure", Phys. Rev. Lett. 95, 074801 (2005)

[19] Comfoltey, E.N. et al. "Design of an overmoded W-band TWT" Vacuum Electronics Conference (IVEC '09). IEEE International, 127-128 (2009)

[20] Young-Min Shin and Larry R. Barnett, Appl. Phys. Lett. 92, 091501 (2008)

[21] Young-Min Shin, Larry R. Barnett, and Neville C. Luhmann Jr., Appl. Phys. Lett. 93, 221504 (2008)

[22] CST Microwave Studio version 2011

[23] J. F. Gitinz, "Power Traveling Wave Tubes", New York, American Elsevier Pub. Co. [1965]

[24] CST Particle-Studio version 2011

Figure Captions

FIG. 1 (a) Conceptual drawing of multi-beam interaction structure (b) structural drawing with dimensional parameters

FIG. 2 (a) 1st order dispersion curves ($\varphi = 1 \sim 3\pi$) of TE_{10}, TE_{20}, and TE_{30} modes with the beam lines at $\varphi = 1.5\pi$ (19.3 kV) and $\varphi = 2.5\pi$ (6.72 kV) (b) phase velocity (bottom) and synchronized beam voltage (bottom) versus frequency graphs on the backward ($\varphi = 1 \sim 2\pi$: LHS) and forward ($\varphi = 2 \sim 3\pi$: RHS) wave synchronous dispersion curves

FIG. 3 (a) Transmission graphs (S21 spectrum) of the 2 mm long structures without (top) and with (bottom) the dielectric plat lattices (b) 3D plots of EM power distribution (mid-plane) of TE_{10}, TE_{20}, and TE_{30} modes at 1 THz (red-dashed in (a))

FIG. 4 Numerical parameter graphs from eigenmode solver simulations (a) cavity impedance (R/Q) and (b) unloaded quality factor (Q_0) versus frequency

FIG. 5 (a) Interaction impedance (K_0) and (b) power growth rate (gain per distance) of backward wave ($\varphi = 1 \sim 2\pi$: top) and forward wave ($\varphi = 2 \sim 3\pi$: RHS) bands of the 1st spatial harmonic dispersion curves, calculated from analytic model (Pierce small signal analysis)

FIG. 6 FDTD-PIC simulation results (a) energy distribution of three electron beams, (b) radiation power (in dBm unit) graphs in time domain, and (c) frequency spectra of three interactive modes (TE_{10}, TE_{20}, and TE_{30})

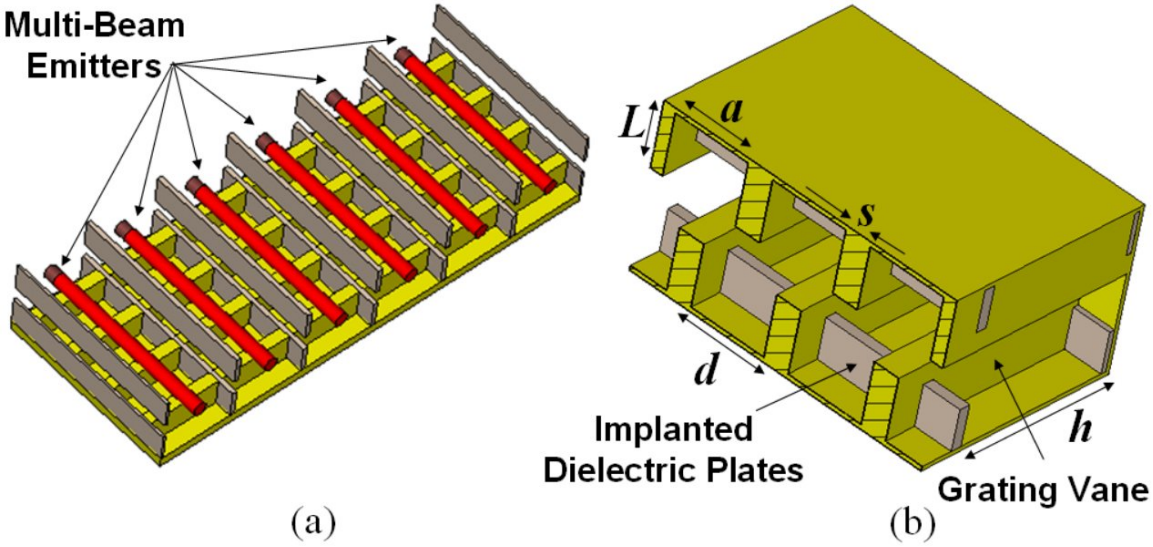

FIG. 1 (Y. M. SHIN)

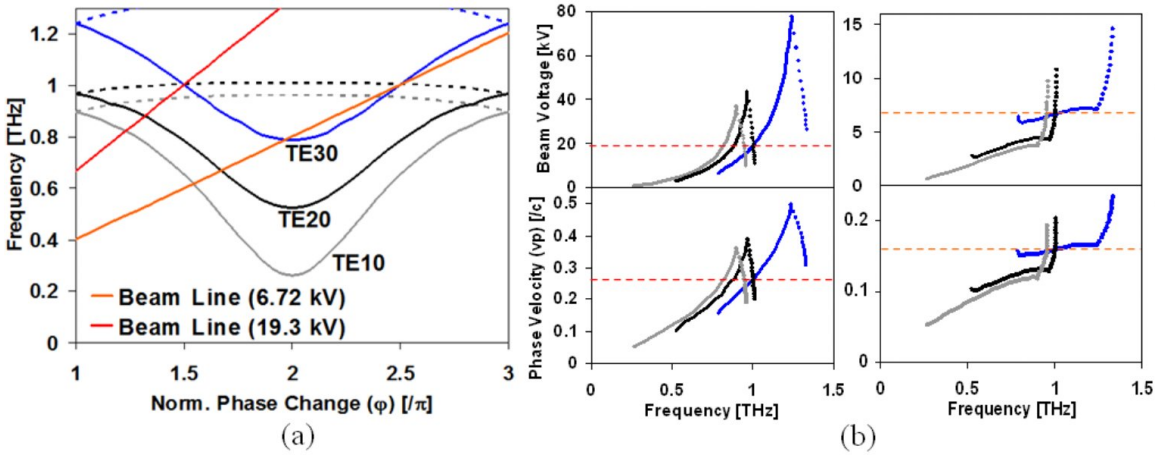

FIG. 2 (Y. M. SHIN)

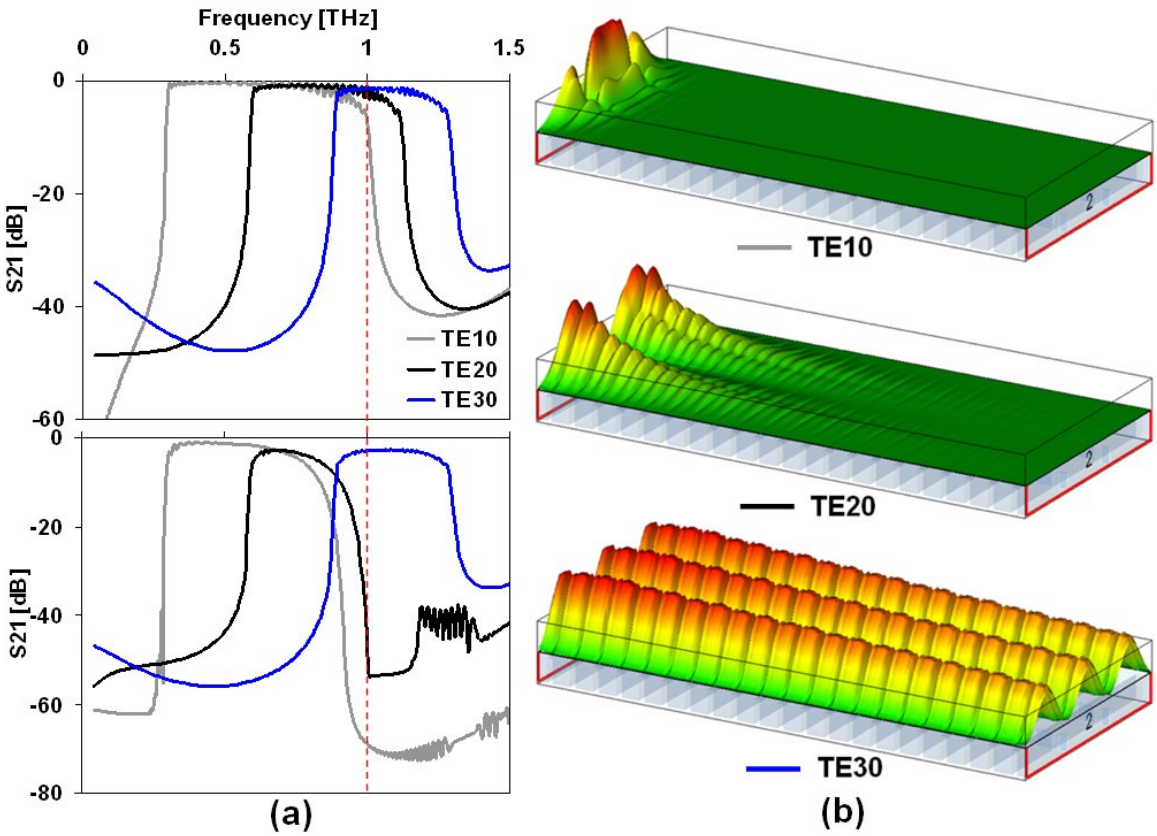

FIG. 3 (Y. M. SHIN)

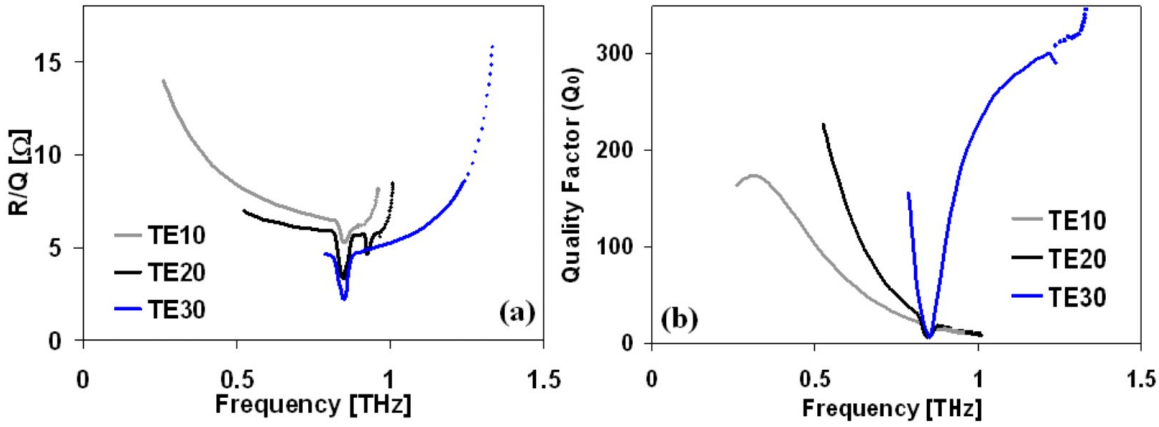

FIG. 4 (Y. M. SHIN)

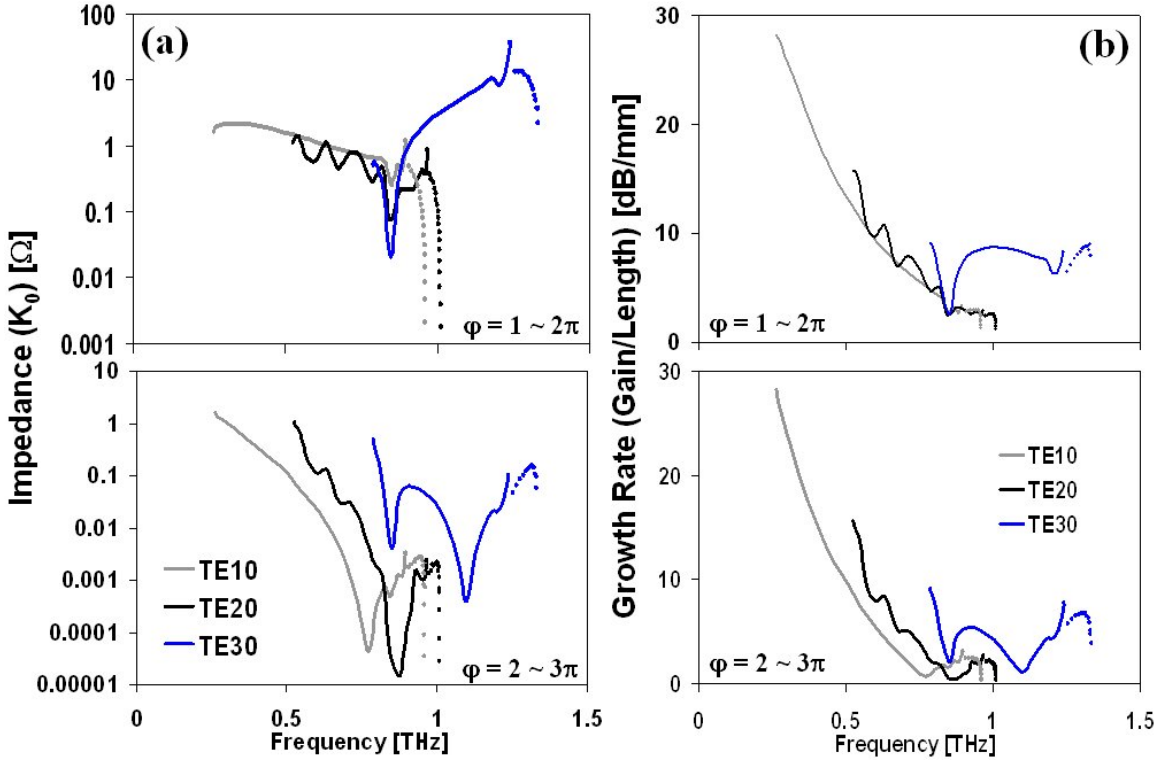

FIG. 5 (Y. M. SHIN)

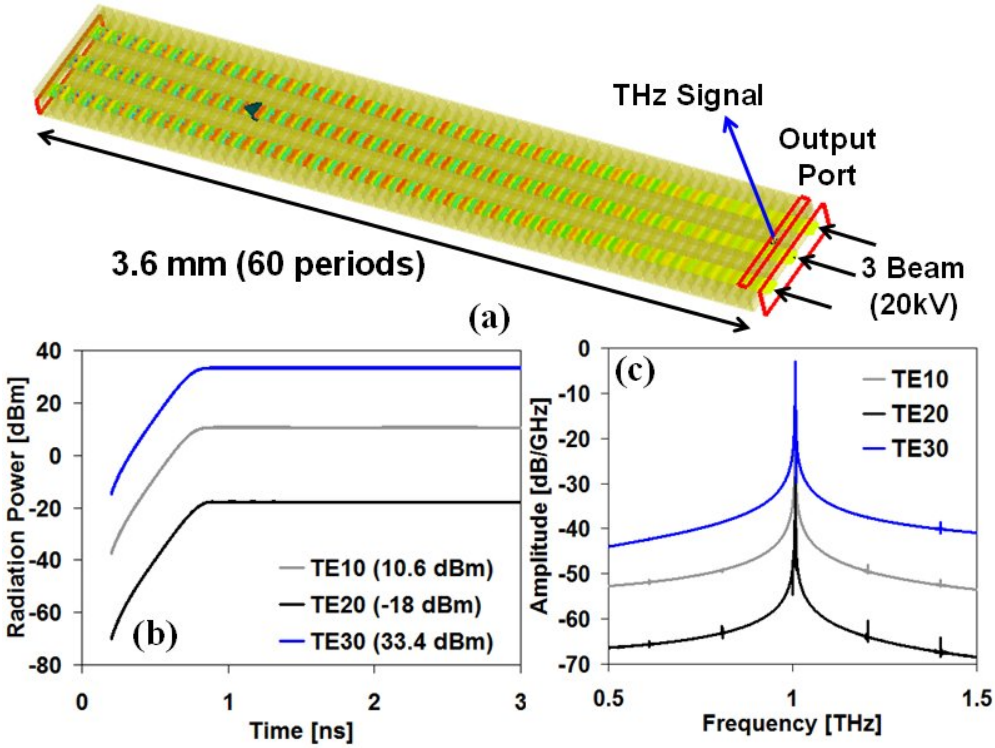

FIG. 6 (Y. M. SHIN)